Pilot-Free VCSEL Temperature Monitoring via Statistical Complexity

Citation for the original published paper (version of record):
Pourafzal, A., Kaimre, H., Häger, C. et al (2026). Pilot-Free VCSEL Temperature Monitoring via Statistical Complexity. IEEE Photonics Journal, In Press.
http://dx.doi.org/10.1109/JPHOT.2026.3669401

Pilot-Free VCSEL Temperature Monitoring via Statistical Complexity

Alireza Pourafzal, *Member, IEEE*, Hans Daniel Kaimre, *Student Member, IEEE*, Christian Häger,
Peter A. Andrekson, *Life Fellow, IEEE*, and Henk Wymeersch, *Fellow, IEEE*

***Abstract*—Vertical-cavity surface-emitting lasers (VCSELs) are the dominant light sources in short-reach optical interconnects, where cost, efficiency, and scalability are critical. However, their modulation bandwidth, output power, and signal integrity degrade markedly as ambient temperature rises and self-heating increases, making accurate device-level temperature awareness indispensable. Existing approaches rely on embedded sensors or forward-voltage monitoring, which require calibration, additional hardware, or pilot overhead, and are therefore not well suited for in-service operation. This work introduces a *pilot-free* and *sensor-free* method for inferring VCSEL operating temperature directly from payload signals. We establish, through an electro–thermal rate-equation model, that temperature rise manifests as a systematic reduction in the entropy of the optical waveform. Leveraging this property, we develop a regression-based estimator that achieves sub-5°C accuracy in simulation. The results demonstrate that entropy-based payload analysis provides a principled and low-cost proxy for junction temperature, with potential for integration into high-speed link management.**

***Index Terms*—VCSEL, optical interconnects, temperature monitoring, entropy, machine learning**

I. INTRODUCTION

Vertical-cavity surface-emitting lasers (VCSELs) at 850–900 nm underpin cost-, power-, and density-critical short-reach interconnects in datacenters and AI accelerators [1]. Their wafer-scale manufacturability, low drive voltage, circular beam, and efficient coupling to multimode fiber make them the default light sources for 50–200 Gb/s lanes in high-radix switches and co-packaged optics [2]. As lane rates and channel counts increase, thermal headroom tightens: temperature variations influence threshold current, differential gain, slope efficiency, output power, modulation response, and emission wavelength [3]. These dependencies are evident in low-temperature operation, where carrier dynamics and recombination rates shift measurably [4], and in long-wavelength multi-quantum-well devices, where lattice-temperature changes alter threshold behavior and spectral position [5]. At the link level, elevated temperature degrades eye quality and increases the likelihood of bit errors at high symbol rates [6]. Such degradations are further aggravated by self-heating within the device and by the thermal impedance of packages and substrates [7].

Accurate knowledge of the instantaneous device temperature, ideally the junction temperature, is essential for margin tracking, adaptive biasing, and equalization, and for preventing thermal runaway in high-speed links [8]. Key VCSEL parameters, including threshold current, slope efficiency, resonance frequency, series resistance, and emission wavelength, vary measurably with temperature [2]. Device measurements over 20–100°C show substantial performance spread and identify thermal design as a first-order constraint beyond 50 Gb/s per lane [9]. While compact electro–thermal models exist to describe roll-over, self-heating dynamics, and bandwidth compression [10], estimating the instantaneous temperature from such models in operation is impractical: it requires detailed knowledge of device-specific parameters and extensive temperature-dependent characterization (such as light-current (L-I) characterization [11], injected current's heat generation [12] and circuit-level electro–opto–thermal formulations [13]). This makes direct, in-situ temperature awareness critical for maintaining link performance and reliability.

Three classes of methods exist for temperature monitoring. *(i) Embedded thermometry* places sensors near the die or uses forward-voltage measurements; these approaches are simple and compatible with digital diagnostic monitoring (DDM)/digital optical monitoring (DOM), but require calibration and can report case/package temperatures that lag the junction under dynamic load [14]. Packaging improvements such as aluminum nitride (AlN) submounts and thermally conductive epoxy can reduce thermal impedance and help limit self-heating [15], but they do not provide a direct temperature measurement. Transient forward-voltage thermometry enables time-resolved thermal-impedance evaluation in VCSEL diodes [16], although it still requires controlled excitation, calibration, and is not generally applicable during live payload operation. *(ii) Spectral thermometry* infers temperature from the wavelength drift of the emitted light; this can be highly accurate, but in practice it requires additional optical filtering or interferometric readout that is uncommon in low-cost Ethernet modules [17]. High-precision interferometric methods, such as fiber Fabry–Perot sensing [18], achieve sub-degree resolution [19] but add optical complexity, alignment sensitivity, and cost. Current-driven thermal modulation of VCSEL wavelength further illustrates the strong temperature–wavelength coupling [20], yet such methods still require calibrated spectral measurement equipment and cannot be implemented unobtrusively during normal link operation. *(iii) Pilot-/training-based thermometry* diverts a fraction of the payload to known sequences or tones to probe and re-tune links. Approaches based on small-signal responses or L–I characterization [21], [22] require controlled, stationary excitation (e.g., L–I sweeps or settled small-signal measurements) and dedicated measurement periods that interrupt normal payload transmission. This overhead reduces effective throughput and limits how

---

This work was supported by the Swedish Foundation for Strategic Research (SSF, HOT-OPTICS Project). *(Corresponding author: Alireza Pourafzal.)*

Alireza Pourafzal, Christian Häger, and Henk Wymeersch are with the Department of Electrical Engineering, Chalmers University of Technology, 41296 Gothenburg, Sweden (e-mail: alireza.pourafzal@chalmers.se; christian.haeger@chalmers.se; henkw@chalmers.se).

Hans Daniel Kaimre and Peter A. Andrekson are with the Photonics Laboratory, Department of Microtechnology and Nanoscience (MC2), Chalmers University of Technology, SE-41296 Gothenburg, Sweden (email: kaimre@chalmers.se; peter.andrekson@chalmers.se).

frequently temperature can be tracked in service, especially in cost- and rate-constrained short-reach links. Machine learning has also been applied to VCSEL modeling [1], digital predistortion [23], and laser temperature control [24], yet these implementations are either pilot-based [1], [23] or rely on closed-loop actuation with dedicated sensors rather than inference from in-band payload signals [24].

In this work, we propose a pilot-free method to estimate a VCSEL's internal temperature from the statistical complexity of its payload-driven optical waveform. Using an electro–thermal rate-equation model with temperature-dependent gain, we establish a theoretical link between finite characteristic temperature of gain, history-dependent dynamics, and observable waveform complexity. Our key insight is that this emergent complexity is captured by entropy measures, providing a direct connection between waveform statistics and temperature. Among practical options, we select Fuzzy entropy [25], which is well suited for short, real-valued, and noisy sequences [26]. It serves as the central feature linking waveform complexity to temperature, enabling pilot-free regression without additional sensors or transmitter data.

Our contributions are: *(i)* Providing a dynamical-systems and entropy-based interpretation of electro–thermal VCSEL dynamics, and deriving testable predictions on how thermal feedback and exogenous noise should affect finite-horizon entropy of the payload-driven optical waveform. *(ii)* Developing a practical, pilot-free temperature estimation pipeline that uses Fuzzy entropy of $P_{\text{opt}}(t)$ as a single feature, including design rules for embedding delay, window length, Fuzzy parameters, and a computational complexity analysis tailored to short-reach links. *(iii)* Validating the framework on a temperature-dependent rate-equation model of an 863 nm VCSEL under 20 Gbps OOK, showing (a) a monotonic Fuzzy-entropy–temperature relation under strong temperature–gain coupling, (b) sub-5°C regression accuracy with Gaussian process regression, and (c) loss of temperature sensitivity when coupling is weak or additive noise dominates, delineating the method's operating regime.

Organization. Section II formulates the electro–thermal VCSEL model with temperature-dependent gain. Section III introduces the complexity framework and entropy feature. Section IV describes the blind, entropy-based temperature estimation pipeline. Section V details simulations and results, and Section VI concludes.

II. VCSEL DYNAMICS AND TEMPERATURE COUPLING

A. Rate-Equation Model with Thermal Feedback

The coupled electro-optical and thermal behavior of a VCSEL is modeled using a system of time-domain rate equations for the carrier density $N(t)$, photon density $S(t)$, and the active region temperature $T(t)$, as [10, Eq. (3)–(5)]

$$\frac{\mathrm{d}N(t)}{\mathrm{d}t} = \frac{\eta_i I(t)}{qV_a} - \frac{N(t)}{\tau_n} - \frac{\Gamma g\big(T(t)\big)\big(N(t)-N_0\big)S(t)}{1+\epsilon S(t)}, \tag{1a}$$

$$\frac{\mathrm{d}S(t)}{\mathrm{d}t} = \frac{\Gamma g\big(T(t)\big)\big(N(t)-N_0\big)S(t)}{1+\epsilon S(t)} + \beta\frac{N(t)}{\tau_n} - \frac{S(t)}{\tau_p}, \tag{1b}$$

$$\frac{\mathrm{d}T(t)}{\mathrm{d}t} = \frac{1}{C_{\text{th}}}\left(P_{\text{in}}(t) - P_{\text{opt}}(t)\right) - \frac{T(t)-T_{\text{amb}}}{C_{\text{th}}Z_{\text{th}}}. \tag{1c}$$

Here, $I(t)$ is the injection current (i.e., the externally applied drive current), η_i the internal quantum efficiency, q the elementary charge, V_a the active region volume, τ_n and τ_p the carrier and photon lifetimes, N_0 the transparency carrier density, Γ the optical confinement factor, $g(T)$ the temperature-dependent differential gain, ϵ the gain compression factor, and β the spontaneous emission coupling factor. We interpret $T(t)$ as the junction temperature $T_j(t)$.

While the internal quantum efficiency η_i exhibits only a weak temperature dependence over the operating range of interest [27], we treat η_i as temperature-independent in this work, since the residual variation is small compared to the dominant thermal feedback captured by $T(t)$ and is highly device-specific. The thermal subsystem is characterized by the thermal capacitance C_{th} and thermal resistance Z_{th}, with T_{amb} denoting the ambient temperature. The units of all variables and parameters used in the VCSEL model are summarized in Table II. The injected electrical and extracted optical powers are given by $P_{\text{in}}(t) = I(t)\,V_{\text{device}}(I(t))$ and

$$P_{\text{opt}}(t) = \eta_{\text{out}}\frac{S(t)\,V_a\,h\nu}{\tau_p}, \tag{2}$$

respectively. This coupled model captures the interplay between carrier injection, recombination, stimulated emission, and the dynamic thermal response driven by the electrical–optical power balance. Specifically, the thermal rate equation in (1c) introduces thermal feedback: the temperature $T(t)$ rises with the net electrical–optical power balance, while the optical power $P_{\text{opt}}(t)$ depends on the photon density $S(t)$. Since the gain is temperature-dependent through $g(T)$, the electrical–optical power balance and the gain form a closed feedback loop. Self-heating reduces $g(T)$, which reduces the photon density $S(t)$ and hence the optical power $P_{\text{opt}}(t)$, altering the heating term in (1c). This coupling induces temperature-dependent memory in the emitted waveform $P_{\text{opt}}(t)$.

The rate–thermal surrogate in (1a)–(1c) is intentionally compact and does not model spatial temperature gradients, modal competition, thermal lensing, or detailed IV/radio-frequency/package parasitics. It is used here to isolate how temperature-dependent feedback shapes short-horizon waveform complexity and to demonstrate the resulting simulation trends; while device-specific calibration and measurement validation are valuable for quantitative thermometry and deployment, as well as for establishing the precise functional mapping (e.g., monotonicity) between temperature and the proposed complexity metrics, they are outside the scope of this work and are left to calibration-driven model refinement.

B. Temperature-Dependent Gain Model

The temperature dependence of the optical gain, $g(T)$, is a key feature in VCSEL modeling. Several models exist in the literature, including differential gain/transparency carrier formulations [9], [28] and empirical rational polynomial fits [29], [30]. A common compact surrogate model, used across semiconductor laser models, is an exponential decay with temperature, capturing the characteristic reduction of

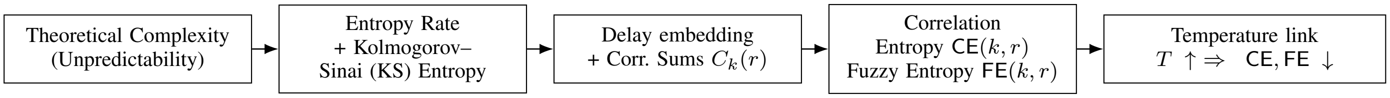

Fig. 1: Roadmap of the theoretical framework: from entropy-based complexity to embedding-based estimators and their temperature trend.

carrier inversion efficiency with a single sensitivity parameter [10], [30]. Following this practice, we adopt the exponential form [31], [32]

$$g(T(t)) = g_0 \exp\left(-\frac{T(t)-T_0}{T_g}\right), \tag{3}$$

where g_0 is the gain at a reference temperature T_0, and T_g is a characteristic temperature parameter describing the device's sensitivity to temperature variations. In practice, T_0 is chosen equal to the nominal ambient temperature at cold start, so that during operation the active-region temperature $T(t)$ starts at T_0 and rises above it due to self-heating. Consequently, the simulations focus on regimes with $T(t) \gtrsim T_0$.

Intuitively, T_g sets the temperature scale over which the differential gain changes noticeably: from (3), a temperature increase ΔT modifies the gain ratio as $g(T_0+\Delta T)/g_0 = \exp(-\Delta T/T_g)$, so an increase $\Delta T = T_g$ reduces g by a factor of e. Devices with smaller T_g are therefore more thermally sensitive (steeper gain roll-off with temperature), whereas larger T_g corresponds to more thermally robust gain.

III. THEORETICAL FRAMEWORK FOR COMPLEXITY ANALYSIS OF VCSEL DYNAMICS

Our observable of interest is a noisy measurement of the optical output $P_{\text{opt}}(t)$. To exploit the emitted waveform as a proxy for temperature, we seek features of $P_{\text{opt}}(t)$ that vary systematically with the thermal state over short observation windows. In this work, we focus on measures of temporal complexity, where complexity denotes how unpredictable an observable time series is given its recent history. In dynamical-systems terms, such behavior is commonly associated with nonlinear feedback and coupling between subsystems, and manifests as history dependence or irregular fluctuations in the output [33], [34].

Entropy-based quantities provide a natural language for characterizing temporal complexity. In particular, we use statistical-complexity notions from computational mechanics to connect the VCSEL electro–thermal dynamics to measurable structure in $P_{\text{opt}}(t)$ (see [35], [36]). In the remainder of this section, we therefore take a brief detour through standard entropy-based tools from dynamical-systems theory and specialize them to this setting: first by introducing the finite-horizon, entropy-rate–like quantities we use, and then by explaining how the temperature coupling in the electro–thermal rate equations is reflected in the resulting entropy-based observable. Fig. 1 summarizes this logical progression of the section. This discussion links the entropy-based definitions to the VCSEL dynamics and motivates the estimators in Sec. IV-A2.

A. Dynamical Entropy and Symbolic Encodings

We view the VCSEL as a discrete-time dynamical system through sampled observations with an internal state and a measured output. Let $x(t) \in \mathcal{X}$ denote the (hidden) state of the device at time t, which in our rate–thermal model collects quantities such as carrier density, photon density, and temperature,

$$x(t) = \big(N(t), S(t), T(t)\big) \in \mathcal{X} \subset \mathbb{R}^3. \tag{4}$$

The experiment does not observe $x(t)$ directly; instead, it records the noisy sampled optical output

$$y_i = P_{\text{opt}}(t_i) + n_i = \mathcal{D}\big(x(t_i)\big) + n_i, \tag{5}$$

where $t_i = i\Delta t$ is the discrete sampling instant with sampling interval Δt, $\mathcal{D} : \mathcal{X} \to \mathbb{R}$ is the measurement function, and n_i collects the effective receiver noise (thermal, shot, and front-end noise) after filtering.

Following the computational–mechanics view of Crutchfield [36], such a dynamical system is characterized by how it combines randomness and structured predictability in its output. The entropy rate quantifies the average randomness per sample in the observed process, while the statistical complexity measures how much information about the past the system must retain internally in order to reproduce the statistics of the output time series [37]. These dynamical-entropy quantities offer a principled way to describe how the carrier–photon–thermal interaction shapes the temporal complexity of $P_{\text{opt}}(t_i)$.

From a theoretical perspective, one could use the entropy rate to quantify how much new information the VCSEL dynamics generate over time. A standard definition for a discrete-time stochastic process is given below.

Definition 1 (Entropy rate). *Let $\{Z_i\}_{i\in\mathbb{Z}}$ be a discrete-time stochastic process taking values in a finite alphabet $\mathcal{Z}$. For $k \in \mathbb{N}$, the length-k block entropy is*

$$H_k(Z) = -\sum_{w\in\mathcal{Z}^k} p(w)\log p(w), \tag{6}$$

where $w = (z_1,\dots,z_k)$ is a word in $\mathcal{Z}^k$ and $p(w)$ is its probability under the process. If the limit exists, the (Shannon) entropy rate is defined as

$$h(Z) = \lim_{k\to\infty} \frac{H_k(Z)}{k}, \tag{7}$$

which represents the average information produced per symbol, including all temporal correlations [36].

In our VCSEL setting, the internal state $x(t)$ is continuous-valued, so it does not directly fit into the finite-alphabet framework above. Moreover, we do not have direct access to $x(t_i)$ but only to the observable y_i. A standard approach in dynamical-systems theory is to introduce a finite measurable partition $\mathcal{P} = \{P_1,\dots,P_M\}$ of the observable range and assign symbols according to $Z_i = j$ whenever $y_i \in P_j$. This observable partition induces a partition of the underlying state space via the preimages $\mathcal{D}^{-1}(P_j)$, so that the resulting symbolic process still reflects the dynamics of the original system when the induced partition is generating [38, Thm. 4.22].[1]

For any fixed partition $\mathcal{P}$, the limit

$$h(Z;\mathcal{P}) = \lim_{k\to\infty} \frac{1}{k} H_k(Z;\mathcal{P}) \tag{8}$$

is the Shannon entropy rate of the symbolic process induced by $\mathcal{P}$. The Kolmogorov–Sinai (KS) entropy of the underlying dynamical system is then defined as

$$h_{\text{KS}} = \sup_{\mathcal{P}} h(Z;\mathcal{P}) = \sup_{\mathcal{P}} \lim_{k\to\infty} \frac{1}{k} H_k(Z;\mathcal{P}), \tag{9}$$

where the supremum is taken over all finite measurable partitions $\mathcal{P}$ of $\mathcal{X}$ [38, Ch. 10]. Thus, KS entropy can be viewed as the largest achievable entropy rate over all finite symbolic codings of the dynamics.

Example: Consider a measured power trace $y_i = P_{\text{opt}}(t_i)$ from the VCSEL. Choose a small set of power intervals, e.g., $P_1 = [0,1)$ mW, $P_2 = [1,2)$ mW, $P_3 = [2,\infty)$ mW, and assign symbols $Z_i \in \{1,2,3\}$ according to the interval containing y_i. For a word length k, we count how often each word $w \in \{1,2,3\}^k$ appears, form empirical probabilities $\hat{p}(w)$, and compute the block entropy $\hat{H}_k(Z;\mathcal{P})$ and $\hat{h}(Z;\mathcal{P})$, from (6) and (8), respectively. Each choice of power partition $\mathcal{P}$ yields one entropy–rate estimate for the resulting symbolic process. To approximate the KS entropy h_{KS}, one would in principle repeat this construction for a sequence of increasingly finer partitions and take the supremum of the corresponding entropy–rate values, as in (9).

B. Embedding-Based Entropy Proxies

The symbolic VCSEL example above illustrates that direct use of h_{KS} as a complexity measure is not practical in our setting. Even for a simple power partition, reliable estimation of the entropy rate requires long, stationary traces and careful control of the binning. In principle, one would then have to repeat this procedure for a sequence of increasingly refined partitions to approximate the supremum in (9). This is difficult because *(i)* finding a partition that is close to generating while still assigning a sufficient number of samples to each bin is nontrivial, and *(ii)* for finite record length and measurement noise, large-k block histograms quickly become ill-posed, since the number of possible words grows as $|\mathcal{Z}|^k$ and many empirical probabilities $p(w)$ are dominated by noise.

A common remedy is to bypass explicit symbolic partitions and reconstruct the dynamics directly from y_i via delay embedding and correlation sums, as outlined below.

1) Delay Embedding and Correlation Sums: Consider a finite observation window of the scalar time series, $\mathcal{Y} = (y_1, y_2, \ldots, y_L)$, and form delay vectors

$$\mathbf{y}_i^{(k)} = \big(y_i,\, y_{i+\tau},\, \ldots,\, y_{i+(k-1)\tau}\big) \in \mathbb{R}^k, \tag{10}$$

with embedding dimension k and integer delay τ (in samples) [39, Thm. 1]. In continuous time, this corresponds to a delay of $\tau\Delta t$, where Δt is the sampling interval.[2]

Recall that block entropies such as H_k in (6) are built from empirical probabilities of length-k "words," typically obtained by counting exact symbol frequencies under a fixed partition. In the correlation-sum approach, symbolic cells are replaced by neighborhoods in the embedded space: rather than counting exact word occurrences, one estimates small-cell probabilities by counting how often delay vectors fall within a metric ball of radius r [40, Eq. (1)],

$$C_k(r) = \frac{2}{(L-k+1)(L-k)} \sum_{i<j} \mathbf{1}\Big\{\mathsf{d}\big(\mathbf{y}_i^{(k)}, \mathbf{y}_j^{(k)}\big) \le r\Big\}, \tag{11}$$

where $\mathsf{d}(\cdot,\cdot)$ denotes a distance (metric) between embedded vectors. For small r, $C_k(r)$ approximates the probability that two independently drawn length-k segments of the trajectory remain within distance r of each other in the embedded space.

From this construction, generalized block entropies can be defined from the scaling of the correlation sums. In particular, the order-2 (Rényi-2) case leads to the so-called *correlation entropy* increment [41, Eq. (11.31)]

$$\mathsf{CE}(k,r) = \ln \frac{C_k(r)}{C_{k+1}(r)}. \tag{12}$$

In the joint limits $k \to \infty$ and $r \to 0$, $\mathsf{CE}(k,r)$ provides a lower bound to the KS entropy h_{KS} [41, Sec. 11.4].

2) Fuzzy Entropy as a Practical Proxy: Direct use of $\mathsf{CE}(k,r)$ with the hard indicator function in (11) is highly sensitive to noise and finite resolution, since small changes around the threshold r can cause large, discontinuous changes in the counts. To address this issue, Pincus [42] and later Chen *et al.* [25] introduced entropy measures that replace the binary neighborhood indicator with a smooth similarity kernel. In particular, *fuzzy entropy* replaces the hard indicator in (11) with a smooth fuzzy kernel [25]

$$\kappa_{n,r}(d) = \exp\Big[-\big(d/r\big)^n\Big], \qquad n \ge 1, \tag{13}$$

and defines the corresponding soft correlation sums

$$\phi_k(r) = \frac{2}{(L-k+1)(L-k)} \sum_{i<j} \kappa_{n,r}\Big(\mathsf{d}\big(\mathbf{y}_i^{(k)}, \mathbf{y}_j^{(k)}\big)\Big), \tag{14}$$

typically with the Chebyshev norm $\mathsf{d}(\mathbf{u},\mathbf{v}) = \max_\ell |u_\ell - v_\ell|$ and with self-matches excluded [25]. Fuzzy entropy is then defined as the corresponding increment

$$\mathsf{FE}(k,r) = \ln \frac{\phi_k(r)}{\phi_{k+1}(r)}. \tag{15}$$

For large n, the kernel $\kappa_{n,r}$ approximates the hard indicator $\mathbf{1}\{d \le r\}$, so $\mathsf{FE}(k,r)$ can be viewed as a smoothed version of $\mathsf{CE}(k,r)$ that is less sensitive to noise and finite sampling.

The discussion in Sections III-A and III-B collects standard notions from nonlinear dynamics, entropy rate, KS entropy, and their finite-data estimators to fix notation and provide a

---

[1] Informally, a partition is generating if the infinite symbol sequence produced by following the trajectory almost uniquely identifies the underlying state. In that case, the symbolic dynamics retains the essential behavior of the original system, including its entropy.

[2] The choice of τ is constrained by the sampling of the underlying continuous dynamics; if τ is too small, successive coordinates are nearly redundant, whereas too large τ risks losing dynamical dependencies.

TABLE I: Comparison of entropy-related quantities for VCSEL dynamics. A check mark (✓) indicates that a property holds, a cross (×) that it does not, and (∼) that it holds under restrictive conditions.

	h	h_{KS}	CE	FE
Computational–mechanics consistency	✓	✓	∼	∼
Requires explicit symbolic partition	✓	✓	×	×
Metric / embedding based	×	×	✓	✓
Provable lower bound to h_{KS}	×	=	✓	∼
Robust to noise / finite resolution	×	×	∼	✓
Practical on short noisy VCSEL traces	×	×	∼	✓
Adopted in this work	×	×	×	✓

common language. These notions are summarized in Table I. In what follows, we use these tools in our contribution, applying them to electro–thermal VCSEL dynamics and showing that Fuzzy entropy of the payload waveform can serve as a pilot-free temperature indicator.

C. Temperature Sensitivity of Correlation-Entropy Measures

We quantify the short-horizon dynamics of the waveform $P_{\text{opt}}(t_i)$ through the close-history event

$$\mathcal{B}_k(r) := \left\{ \mathsf{d}\big(\mathbf{y}_i^{(k)}, \mathbf{y}_j^{(k)}\big) \le r \right\}, \tag{16}$$

with $\mathbf{y}_i^{(k)}$ defined in (10). The hard correlation sum $C_k(r)$ in (11) is the empirical frequency of $\mathcal{B}_k(r)$ pairs. Assuming $\{y_i\}$ is stationary and ergodic, the time average in (11) converges almost surely to its ensemble average. In particular, for fixed (k, r) [41, Sec. 11.3],

$$C_k(r) \xrightarrow[L\to\infty]{\text{a.s.}} \mathbb{E}\Big[\mathbf{1}\Big\{\mathsf{d}\big(\mathbf{y}_i^{(k)}, \mathbf{y}_j^{(k)}\big) \le r\Big\}\Big] = \mathbb{P}\big(\mathcal{B}_k(r)\big). \tag{17}$$

Therefore,

$$\frac{C_{k+1}(r)}{C_k(r)} \to \mathbb{P}\big(\mathcal{B}_{k+1}(r) \mid \mathcal{B}_k(r)\big), \tag{18}$$

and the correlation-entropy increment (12) admits the conditional-probability form

$$\mathsf{CE}(k, r) = \ln \frac{C_k(r)}{C_{k+1}(r)} \approx -\ln \mathbb{P}\big(\mathcal{B}_{k+1}(r) \mid \mathcal{B}_k(r)\big), \tag{19}$$

with the approximation reflecting finite-L estimation.

Next, we connect $\mathcal{B}_k(r)$ to temperature. In the noiseless deterministic setting, Takens' embedding theorem implies that for sufficiently large k the delay map induced by the scalar observable $y(t) = P_{\text{opt}}(t)$ is one-to-one on the attractor generated by the VCSEL dynamics [41, Sec. 3.2]. Hence, on the attractor, each delay vector $\mathbf{y}_i^{(k)}$ identifies a unique internal state $(N(t_i), S(t_i), T(t_i))$ and thus a unique temperature $T(t_i)$. Moreover, the inverse map is continuous on the compact attractor, so for any $\varepsilon > 0$ there exists $r_\varepsilon > 0$ such that [43, Th. 13.92]

$$\mathsf{d}\big(\mathbf{y}_i^{(k)}, \mathbf{y}_j^{(k)}\big) \le r_\varepsilon \implies |T(t_i) - T(t_j)| \le \varepsilon. \tag{20}$$

Equation (20) formalizes the sense in which, at sufficiently small scales, $\mathcal{B}_k(r)$ selects pairs of histories with matched thermal states. The following remark summarizes when this conclusion holds beyond the specific rate–thermal model.

Remark 1 (Conditions for temperature informativeness)**.** *If, for sufficiently large k, the delay map associated with the observable $y(t)$ is one-to-one on the invariant set visited in steady operation (e.g., the attractor), then $T(t_i)$ is a well-defined function of the delay history $\mathbf{y}_i^{(k)}$ (and nearby delay histories correspond to nearby temperatures, cf.* (20)*). Under this observability condition, any temperature dependence in the device dynamics and/or the measurement map $\mathcal{D}$ makes the close-history statistics $\mathcal{B}_k(r)$ and the increments $\mathsf{CE}(k, r)$ (and $\mathsf{FE}(k, r)$) sensitive to operating temperature. This conclusion is structural and does not rely on our specific rate-equation surrogate or on a particular functional form of $g(T)$.*

Event $\mathcal{B}_k(r)$ selects pairs of recent power histories that are similar over a window of length $(k-1)\tau\Delta t$, i.e., they imply similar recent dissipation in the device. Since junction temperature is a slow thermal-RC state driven by this dissipation, such histories correspond to nearly the same instantaneous $T(t_i)$ on the operating attractor, consistent with (20).

D. Correlation Entropy Under Decreasing $g(T)$

We now specialize to the rate–thermal model (1a)–(1c) with $g(T)$ given by (3). Since $g(T)$ decreases with temperature,

$$T\uparrow \quad\Rightarrow\quad g(T)\downarrow, \tag{21}$$

the stimulated-emission terms in (1a)–(1b) are reduced and the carrier–photon subsystem becomes less responsive to small perturbations in the state over a fixed sampling interval. To link (3) to short-horizon persistence, consider the one-step evolution of small perturbations around an operating point on the attractor. Linearizing (1a)–(1c) gives

$$\delta\dot{x}(t) = J\big(x(t), T(t)\big)\, \delta x(t), \tag{22}$$

where J is the Jacobian of the rate–thermal vector field. Over one sampling interval, a first-order (Euler) discretization of the linearized dynamics (22) yields the discrete-time perturbation update $\delta x_{i+1} \approx A(T_i)\, \delta x_i$, where $A(T_i) := \mathbf{I}_3 + \Delta t\, J\big(x_i, T_i\big) \in \mathbb{R}^{3\times 3}$, and $\mathbf{I} \in \mathbb{R}^{3\times 3}$ is the identity matrix. The noiseless optical sample is $y_i = \mathcal{D}(x_i)$, so $\delta y_{i+1} \approx \nabla\mathcal{D}(x_{i+1})^\top \delta x_{i+1}$ and

$$|\delta y_{i+1}| \le c_{\mathcal{D}}\, \|A(T_i)\|\, \|\delta x_i\|, \tag{23}$$

where $c_{\mathcal{D}} := \sup_{x\in A} \|\nabla\mathcal{D}(x)\|$. In (1a)–(1b), the stimulated-emission coupling terms are proportional to $g(T)$, so the dominant gain-dependent entries of J scale with $g(T)$ up to bounded state factors. With $g(T)$ decreasing in T by (3), the induced norm $\|A(T_i)\|$ (and thus the local input–output sensitivity in (23)) decreases with operating temperature, consistent with standard small-signal behavior where reduced differential gain lowers the relaxation-resonance scale and effective modulation bandwidth [10], [31], [32]. Therefore, for fixed (k, τ, r) in the device-dominated regime, the waveform exhibits stronger short-horizon persistence at higher operating temperature, in the sense that

$$T\uparrow \quad\Rightarrow\quad \mathbb{P}\big(\mathcal{B}_{k+1}(r) \mid \mathcal{B}_k(r)\big)\uparrow. \tag{24}$$

Using the conditional-probability representation (19), this yields the trend $T\uparrow \quad\Rightarrow\quad \mathsf{CE}(k, r)\downarrow$.

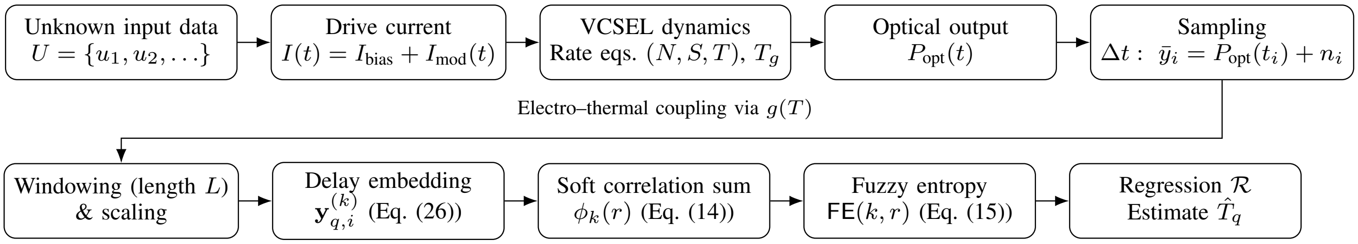

Fig. 2: Blind entropy-based temperature estimation pipeline, from unknown input bits to temperature estimate $\hat{T}_q$.

E. Noise-Robust Persistence via Fuzzy Entropy

In practice, the observed samples satisfy $y_i = P_{\text{opt}}(t_i) + n_i$. Since $C_k(r)$ in (11) relies on the hard test $\mathbf{1}\{\mathsf{d}(\mathbf{y}_i^{(k)}, \mathbf{y}_j^{(k)}) \leq r\}$, noise can toggle near-threshold pairs across r, causing large variations in $C_k(r)$ and degrading the finite-sample estimate $\mathsf{CE}(k, r)$ at the small radii required to probe local predictability. We therefore use $\mathsf{FE}(k, r)$ (Section III-B), which replaces the indicator by the smooth kernel $\kappa_{n,r}(\cdot)$ and computes the same log-ratio from the corresponding soft correlation sums $\phi_k(r)$. Thus, $\mathsf{FE}(k, r)$ retains the conditional-persistence interpretation of $\mathsf{CE}(k, r)$, but with soft neighborhood membership: it quantifies how much the average similarity of length-k histories is preserved when extending them to length $k+1$. As $n \to \infty$ the kernel $\kappa_{n,r}$ approaches the hard indicator and $\mathsf{FE}(k, r) \to \mathsf{CE}(k, r)$ (for fixed r).

Remark 2 (Role of exogenous variability)**.** *In real links, exogenous variability (receiver noise/jitter, temperature-sensitive electronics, and packaging effects) perturbs the observed histories, reducing the effective persistence of nearby trajectories. In the conditional form* (19)*, this corresponds to a decrease in the probability that two close k-histories remain close when extended by one sample, i.e., a decrease of* $\mathbb{P}(\mathcal{B}_{k+1}(r) \mid \mathcal{B}_k(r))$*, which increases the measured entropy proxy. Consequently, the observed* $\mathsf{FE}(k, r)$ *reflects a competition between deterministic thermal structure in the VCSEL dynamics (tending to lower* FE*) and stochastic perturbations (tending to raise* FE*). The net trend depends on SNR and the history window* $(k-1)\tau\Delta t$ *relative to* τ_{th}.

This theoretical link between thermal feedback and entropy motivates our practical framework for blind temperature estimation from payload waveforms, in the subsequent section.

IV. BLIND TEMPERATURE ESTIMATION APPROACH

The proposed blind temperature estimation method operates directly on the observed VCSEL output power and requires no pilot symbols or a priori knowledge of the transmitted data. The approach consists of three main steps: *(i)* transmitting data through the VCSEL and recording the resulting optical power sequence $P_{\text{opt}}(t)$; *(ii)* extracting the Fuzzy entropy of the observed output as a quantitative feature of signal complexity; and *(iii)* estimating the internal temperature by applying a regression model to the computed entropy value. Each of these steps is described in detail in the following subsections, and the overall estimation pipeline is summarized in Fig. 2.

A. Temperature Estimation Pipeline

1) Data Acquisition and Signal Model: Let $U = \{u_1, u_2, \dots\}$ denote a discrete sequence of transmitted data symbols, with $u_i \in \mathcal{A}_u = \{0, 1\}$ for the case of PAM-2 modulation considered in this work. The data sequence is mapped to a modulated current $I_{\text{mod}}(t)$, which is superimposed on a fixed bias current I_{bias} to form the total drive current applied to the VCSEL:

$$I(t) = I_{\text{bias}} + I_{\text{mod}}(t). \tag{25}$$

The current $I(t)$ governs the carrier and photon dynamics within the VCSEL via the nonlinear rate equations and associated thermal feedback. The modulated optical output of the VCSEL is characterized by the photon density $S(t)$, which is converted to optical power $P_{\text{opt}}(t)$ according to the established system parameters, as detailed in Section II-A. At the receiver, only the time series $P_{\text{opt}}(t)$ is accessible;[3] the original data U and internal state variables (N, S, T) are unobserved.

2) Feature Extraction: The received waveform at the input is modeled as a noisy observation of the VCSEL optical output, as $\bar{y}_i = P_{\text{opt}}(t_i) + n_i$, where $P_{\text{opt}}(t_i)$ is the sampled optical power (up to the deterministic front-end gain). The sequence $\{\bar{y}_i\}$ is uniformly sampled with sampling period Δt and then segmented into Q non-overlapping windows of length L. For window index $q \in \{1, \dots, Q\}$ we define $\bar{\mathcal{Y}}_q = (\bar{y}_{(q-1)L+1}, \dots, \bar{y}_{qL})$. If a local index $\ell \in \{1, \dots, L\}$ is convenient, we write $\bar{y}_{q,\ell} := \bar{y}_{(q-1)L+\ell}$. We choose L such that the thermal state $T(t)$ is approximately constant within a window, i.e., $L\,\Delta t \ll \tau_{\text{th}}$, while still satisfying $(k-1)\tau \ll L$ (such that $L\Delta t$ spans at most a small fraction (e.g., 0.05–0.1) of τ_{th}). This local quasi-stationarity justifies estimating a short-horizon entropy-based complexity measure (the Fuzzy entropy FE) per window and mapping it to an instantaneous temperature label.

Within each window, we apply peak normalization,

$$\mathcal{Y}_q = \frac{\bar{\mathcal{Y}}_q}{m_q}, \qquad m_q = \max_i |\bar{y}_{q,i}|,$$

which keeps the waveform shape intact and makes the tolerance r interpretable in normalized units. This simple scaling avoids altering the statistics too much while compensating for unknown front-end gain.

---

[3] In practice, the receiver accesses this quantity indirectly: the optical power at the VCSEL facet (as $P_{\text{opt}}(t)$ in (2)) incident on a photodiode generates a photocurrent $I_{\text{PD}}(t) = R\,P_{\text{opt}}(t)$, with detector responsivity R, and followed by electrical amplification. The measured signal is linearly proportional to $P_{\text{opt}}(t)$, up to front-end bandwidth and noise [44, Sec. 4.3].

Further, we form k-dimensional delay vectors with lag τ (in samples),

$$\mathbf{y}_{q,i}^{(k)} = \big(y_{q,i},\, y_{q,i+\tau},\, \dots,\, y_{q,i+(k-1)\tau}\big), \tag{26}$$

where $1 \le i \le L-(k-1)\tau$. From these vectors we compute the Fuzzy-entropy increment $F_q = \mathsf{FE}(k,r)$ using (13)–(15), with self-matches excluded as in standard definitions.

3) Regression-Based Temperature Estimation: The final stage of the framework is supervised regression, mapping the extracted Fuzzy entropy features to temperature estimates. Given the dataset of tuples $\{(F_q, T_q)\}_{q=1}^{Q}$, the regression problem is to learn a mapping

$$\hat{T}_q = \mathcal{R}(F_q),$$

where $\mathcal{R} : \mathbb{R} \to \mathbb{R}$ predicts temperature from the Fuzzy entropy feature. The regressor $\mathcal{R}$ is trained using a labeled dataset, minimizing the prediction error over all training pairs.

The choice of regression model is addressed in the implementation section. Once trained, the model is applied in operation: for each newly acquired window of $\bar{\mathcal{Y}}$, Fuzzy entropy is computed and input to $\mathcal{R}$ to yield a pilot-free estimate of the internal VCSEL temperature.

B. Design Choices and Defaults

1) Delay τ selection: A suitable delay τ is required to construct informative delay vectors (26). Choosing the smallest delay $\tau = 1$ is generally suboptimal when the sampling interval Δt is small relative to the dominant time scales of the dynamics: then $y_{i+1} \approx y_i$ and successive embedding coordinates are nearly redundant, leading to poorly conditioned reconstructions. Following standard practice, we adopt the average mutual information (AMI) criterion, which selects τ as the first local minimum of [45, Eq. (9)]

$$\mathsf{MI}(\tau) \;=\; \sum_{a,b} p_{ab}(\tau)\, \ln \frac{p_{ab}(\tau)}{p_a\, p_b}, \tag{27}$$

between y_i and $y_{i+\tau}$, where $p_{ab}(\tau)$ is the joint probability that y_i falls in bin a and $y_{i+\tau}$ in bin b, and p_a, p_b are the corresponding marginals. The exact bin resolution affects the absolute value of $\mathsf{MI}(\tau)$, but the location of its first minimum is typically robust and is used here as the embedding delay.

Since $\mathsf{MI}(\tau)$ quantifies the deviation of the joint law $p_{ab}(\tau)$ from independence ($p_a p_b$), the first minimum identifies the smallest delay (i.e., smallest $\tau\Delta t$) for which this deviation, and thus redundancy between coordinates, has dropped substantially while the dependence is not lost entirely; this yields embedding coordinates that are informative without being trivially correlated [41, Sec. 9.2].

2) Fuzzy parameters: Fuzzy entropy requires three parameters: the embedding dimension k, the tolerance r, and the fuzziness exponent n [25]. The embedding dimension k specifies the length of the delay vectors used in the entropy calculation. While higher dimensions may in principle capture more structure, they rapidly increase computational complexity (cf. Sec. IV-C) and reduce the number of usable vectors. We therefore restrict to a compact set $k = 2$–5. The tolerance r determines the width of the similarity boundary and is scaled to σ_y, the standard deviation of the windowed signal, as $r = c\,\sigma_y$, with c typically in the range 0.1–0.3. The exponent n controls the steepness of the fuzzy kernel: larger n approximates a hard threshold, whereas smaller n increases smoothing. Recommended values are integers $n = 2$–5 [25]. The parameters (k, r, n) are selected by validation, choosing the smallest values that yield stable FE across adjacent window sizes (cf. Sec. IV-A2).

3) Window length L: The window length balances two opposing needs: (i) *quasi-stationarity* of the thermal state within the window, and (ii) *sufficient samples* for a stable Fuzzy-entropy estimate. Quasi-stationarity is required because drift of the thermal state (and hence device parameters) within a window makes the assigned temperature label ambiguous and violates the stationary-manifold assumption underlying delay-embedding-based entropy estimates, cf. Takens' theorem [41, Sec. 3.2]. We therefore require the window duration to be short compared to the thermal time constant, $L\Delta t \ll \tau_{\text{th}}$.[4]

The choice of L is guided by discriminability across temperature conditions. We evaluate FE over a grid of candidate window sizes and track (i) the mean separation between adjacent temperature classes and (ii) the across-run variance, in the spirit of Fisher-type separation [46, Sec. 4.1.4]. We then select the smallest $L^{\star}$ for which the variance is sufficiently low and further increases yield only marginal improvements in class separation. This approach ensures a balance between discrimination power and computational efficiency.

4) Estimating τ_{th}: If τ_{th} is unknown, we estimate an effective $\hat{\tau}_{\text{th}}$ from a small step test. Starting cold/off at $T(0){=}T_{\text{amb}}$, apply a constant bias I_{bias} at $t{=}0$ for a short interval (e.g., $1\,\mu$s), and record the instantaneous temperature. The thermal response is well-approximated by a first-order exponential rise

$$\Delta T(t) \;\approx\; \Delta T_{\infty}\Big(1 - e^{-t/\tau_{\text{th}}}\Big),$$

where $\Delta T_{\infty} = T(\infty) - T_{\text{amb}}$ is the steady-state temperature increase for the applied step. In practice the full asymptote may not be observed in a short record; $\hat{\tau}_{\text{th}}$ is then obtained by fitting the measured trajectory $\Delta T(t)$ to the exponential model. We fit the model $\Delta T(t) \approx A(1 - e^{-t/\tau})$ to the recorded samples by nonlinear least squares, initialized with $A \approx \Delta T(t_{\text{end}})$ and a plausible τ. The fit directly yields $\hat{A} = \Delta T_{\infty}$ and $\hat{\tau} = \tau_{\text{th}}$, and remains reliable even if the record does not reach steady state, since τ is identified from the transient curvature.

C. Computational Complexity

The computational cost of the Fuzzy-entropy estimator is dominated by three steps: (i) constructing the embeddings $\mathbf{Y}_{k,q} = [\mathbf{y}_{q,1}^{(k)}, \mathbf{y}_{q,2}^{(k)}, \dots, \mathbf{y}_{q,M_k}^{(k)}] \in \mathbb{R}^{M_k \times k}$, where $M_k = L - (k-1)\tau$ and $\mathbf{Y}_{k+1} \in \mathbb{R}^{M_{k+1}\times(k+1)}$, which requires $\mathcal{O}(M_k k + M_{k+1}(k{+}1))$ operations; (ii) forming the full pairwise Chebyshev distances, costing $\mathcal{O}(M_k^2 k + M_{k+1}^2(k{+}1))$; and (iii) applying the fuzzy kernel and averaging in (14), with complexity $\mathcal{O}(M_k^2 + M_{k+1}^2)$. Thus the overall time complexity

---

[4] In a first-order lumped thermal model, the junction temperature relaxes exponentially to a steady value on the scale τ_{th}, so choosing $L\Delta t \ll \tau_{\text{th}}$ keeps $T(t)$ approximately constant within each window [9].

is $\mathcal{O}(M_k^2 k + M_{k+1}^2(k+1))$, which in the common regime $M_k, M_{k+1} = \Theta(L)$ reduces to $\mathcal{O}(kL^2)$ per window. Memory usage is likewise quadratic, $\mathcal{O}(M_k^2 + M_{k+1}^2)$, as both distance matrices must be stored.

D. System-Level Integration and Practical Considerations

The proposed entropy-based estimator is designed to integrate seamlessly into existing optical receiver architectures. In practical implementations, the estimator operates on waveform samples that are already available within the digital signal processing chain. Modern optical receivers routinely process oversampled electrical waveforms for tasks such as clock recovery, timing adjustment, and equalization prior to symbol decisions [44, Sec. 4.3]. The entropy features are extracted from windowed segments of length L chosen such that $L\Delta t \ll \tau_{\text{th}}$. Consequently, temperature estimates are produced at an update rate on the order of $(L\Delta t)^{-1}$, which is orders of magnitude lower than the symbol rate and governed by the thermal dynamics than by the communication bandwidth.

The resulting junction-temperature estimate $\hat{T}(t)$ can be interpreted as a latent device-state observation that is otherwise inaccessible during normal link operation. Exposing this state enables the estimator to serve as an input to higher-level monitoring and control functions without requiring protocol modification or additional sensing hardware. At the transmitter side, temperature awareness is commonly exploited through closed-loop or supervisory control mechanisms that compensate slow thermal drift in directly modulated VCSELs. In practice, such compensation is achieved by adapting the bias current and modulation amplitude to stabilize average optical power and extinction ratio across temperature, as implemented in adaptive optical power control (APC) and auto-modulation control (AMC) architectures for VCSEL drivers [47]. In this setting, the estimated junction temperature $\hat{T}(t)$ provides an explicit and physically meaningful state input to existing APC/AMC loops, replacing or complementing indirect proxies without requiring back-facet monitoring or transmitter-side instrumentation [48].

Beyond immediate drive adaptation, junction-temperature estimates also enable thermal derating and reliability-aware operation at the system level. Junction temperature is a primary driver of aging, degradation, and failure mechanisms in semiconductor lasers, with sustained high-temperature operation accelerating wear-out and reducing device lifetime [49, Ch. 1]. Leveraging this dependence, $\hat{T}(t)$ can be used to enforce operating envelopes that limit cumulative thermal stress, e.g., by reducing modulation depth or invoking higher-layer data-rate adaptation under prolonged thermal load. Such derating policies are natural system-level responses to temperature-induced performance constraints in semiconductor lasers [50, Ch. 7]. Along the same lines, reliability studies commonly infer degradation-relevant states from electrical or optical observables when direct sensing is unavailable [51].

In short-reach VCSEL interconnects (e.g., data-center links), temperature variations similarly motivate adaptive operation (e.g., modulation/waveform/coding selection) to sustain throughput across operating conditions [1]. At a larger scale, $\hat{T}(t)$ can be treated as a low-rate telemetry signal and incorporated into optical performance monitoring and control frameworks, where slowly varying physical-layer state information is reported intermittently and used for supervision, margin management, and fault detection [52].

TABLE II: Key simulation and device parameters (Ohiso-based VCSEL [53], exponential $g(T)$).

Parameter	**Value**
Wavelength λ	863 nm
Internal quantum efficiency η_i	1.0
Spontaneous emission factor β	1×10^{-4}
Carrier lifetime τ_n	5 ns
Photon lifetime τ_p	2.28 ps
Transparency carrier density N_0	$1.94 \times 10^{24}\ \mathrm{m}^{-3}$
Differential gain at T_0 g_0	$1 \times 10^{-7}\ \mathrm{m}^3/\mathrm{s}$
Gain reference temperature T_0	300 K
Gain compression ϵ	1×10^{-16}
Confinement factor Γ	0.3
Active region volume V_a	$3 \times 10^{-17}\ \mathrm{m}^3$
Thermal impedance Z_{th}	2.6×10^{3} K/W
Thermal capacitance C_{th}	1×10^{-5} J/K
Thermal time constant τ_{th}	2.6×10^{-2} s
Output coupling η_{out}	0.45
Bias current I_{bias}	20 mA
Modulation amplitude I_{mod}	5 mA
Bit rate	20 Gbps
Oversampling factor	25
Photodiode responsivity R_{PD}	0.6 A/W
Load resistance R_L	$50\ \Omega$
Receiver bandwidth Δf	20 GHz

V. SIMULATION IMPLEMENTATION AND RESULTS

A. Environment and Model Setup

We simulate the coupled carrier–photon–thermal dynamics using the rate-equation model in Sec. II-A with the exponential temperature-dependent gain of (3). Device and simulation parameters are given in Table II.

B. Small-Signal (Steady-State) Simulations

In the steady-state regime, the modulation current is set to zero and the bias current I_{bias} is swept from 0 to 40 mA for each combination of[5]

$$T_g \in \{50,\ 250,\ 500\}\ \text{K}, \quad T_{\text{amb}} \in \{25,\ 90\}\ ^\circ\text{C}.$$

The instantaneous device voltage $V(I)$ is computed from the empirical IV fit in [10], and the injected electrical power is $P_{\text{in}}(t) = I(t)\,V(I(t))$. The steady-state optical output power $P_{\text{opt}}(t)$ is obtained from the simulated photon density $S(t)$ as in (2).

Fig. 3 illustrates the exponential fitting procedure of Sec. IV-B4. The observation window must be long enough to capture the transient curvature; convergence to the true $\tau_{\text{th}} = C_{\text{th}} Z_{\text{th}}$ is reached once the window exceeds $10\,\mu$s. Based on this, for subsequent small-signal simulations we set the observation window to $10\,\mu$s, which provides stable

---

[5] Characteristic temperatures on the order of $T_g \approx 100$ K have been reported for laser diodes using temperature-dependent rate-equation models [31]. We use the sweep $\{50, 250, 500\}$ K to cover strong, moderate, and weak coupling regimes around this reference scale.

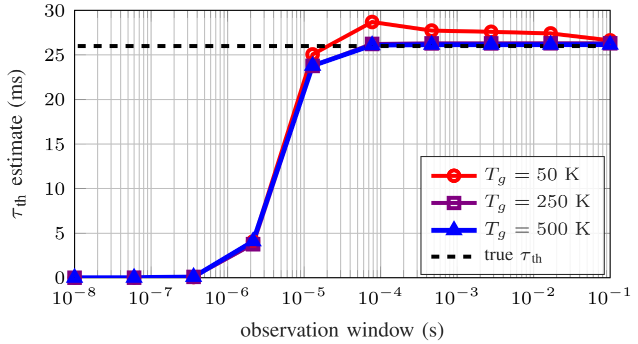

Fig. 3: Estimated thermal time constant τ_{th} as a function of observation window length for different gain–temperature parameters T_g.

τ_{th} estimation while keeping simulation runtime short, and ensures that carrier, photon, and thermal states converge to steady values. This duration is consistent with the device's thermal time constant (see Table II).

Figure 4 shows optical output power and photon density versus I_{bias} for different T_g and T_{amb}. Lower T_g increases the gain's temperature sensitivity, strengthening the coupling between self-heating and photon generation. At $T_g = 50$ K, both quantities exhibit pronounced roll-over with increasing I_{bias}, especially at higher T_{amb}, due to rapid gain suppression. Larger T_g values yield near-linear behavior over the bias range, indicating weaker thermal feedback and delayed roll-over.

At $I_{\text{bias}} = 20$ mA and $T_{\text{amb}} = 25$°C, Fig. 5 presents a parametric sensitivity study with respect to the gain characteristic temperature T_g in (3). Since T_g is a device/material parameter, this sweep should be interpreted as comparing VCSELs (or process/design variants) with different gain–temperature roll-off, rather than tuning a knob on a fixed device. In the model, smaller T_g implies stronger degradation of $g(T)$ for a given junction temperature, which reduces stimulated emission and lowers the steady optical power generated under the same drive. The reduced optical extraction implies a slightly larger fraction of the injected electrical power is dissipated internally, leading to a modest increase in the junction temperature. Consistent with this mechanism, as T_g increases (weaker gain penalty), the optical power (blue circles) rises from ≈ 4.5 to ≈ 7 mW, while the junction temperature (red squares) decreases slightly from ≈ 55.1°C to ≈ 54.85°C.

C. Large-Signal Simulations

For dynamic analysis, we fix $I_{\text{bias}} = 20$ mA and set $I_{\text{mod}} = 5$ mA. A binary frame of 12,144 bits (IEEE 802.3 LAN test length [54]) is transmitted at 20 Gbps with oversampling factor (OSF) 25 for ordinary differential equation (ODE) integration. Current levels are $I_0 = I_{\text{bias}} - I_{\text{mod}}/2$ and $I_1 = I_{\text{bias}} + I_{\text{mod}}/2$. At the receiver, a responsivity-R_{PD} photodiode converts optical power to current, followed by an ideal low-pass front end of bandwidth $\Delta f = 20$ GHz and additive thermal and shot noise: $\sigma^2_{i,\text{th}} = 4k_B T_{\text{amb}} \Delta f / R_L$ and $\sigma^2_{i,\text{sh}} = 2q\,\bar{i}_{\text{PD}} \Delta f$ which results in a signal-to-noise ratio (SNR) of approximately 38 dB in the default configuration. A fixed threshold detector is used, no adaptive equalization, timing recovery, or decision feedback (since our goal is to capture relative trends with temperature and T_g, not to emulate a fully equalized Ethernet link.). Each configuration is repeated over 25 Monte Carlo runs (random data and noise seeds).

TABLE III: Parameters for Fuzzy-entropy Complexity Estimation.

Parameter	Value
Embedding delay τ	$\tau^\star \approx 0.30$ sym.
Embedding dim. k	2
Fuzzy exponent n	3
Tolerance r	$0.2\sigma_y$
Window length L	128 bits

Figure 6 contrasts strong gain–temperature coupling ($T_g = 50$ K) and weak coupling ($T_g = 500$ K) at $T_{\text{amb}} \in \{20°\text{C}, 95°\text{C}\}$. Under strong coupling, the gain term $g(T)$ is more strongly suppressed at elevated temperature, which reduces the effective differential gain and slows the carrier–photon response over the bit interval. The resulting slower transitions and run-length dependence increase deterministic inter-symbol interference (ISI) and compress the decision margin, reducing the eye opening from $\Delta P \approx 0.40$ to ≈ 0.16 mW when raising T_{amb} from 20°C to 95°C. Under weak coupling, $g(T)$ varies less with temperature, so the transition dynamics and rail levels remain more stable, and the eye opening only reduces from ≈ 0.40 to ≈ 0.34 mW at 95°C. This behavior is consistent with the bit error rate (BER) trends in Fig. 7.

Figure 7 reports BER versus initial ambient temperature. BER increases monotonically with temperature for $T_g = 50$ K, reflecting stronger gain–temperature coupling: higher T suppresses $g(T)$, deepens pattern-dependent ISI, and widens the decision margin loss. For $T_g = 500$ K, BER varies only mildly with temperature, consistent with weaker thermal feedback and a more linear response.[6]

D. Dynamical Complexity Analysis

We select parameters for complexity estimation: the embedding delay τ, Fuzzy-entropy settings (k, r, n), and the window length L. Following Sec. IV-A2, τ is obtained via the AMI criterion. As shown in Fig. 8, the AMI curves decay consistently across OSFs, with the first minimum at $\tau^\star \approx 0.30$ symbols (about 7 samples at OSF$=25$), which we use in all experiments. We fix $k = 2$, $n = 3$, and $r = 0.2\sigma_y$ based on pilot tuning; detailed sweeps are omitted for brevity. The window length L is chosen using Fig. 9. We select the smallest L for which the variance is stable and the mean separation between temperature classes is clear. With $L = 128$ bits at 20 Gbps, the window duration is $L\Delta t \approx 6.4$ ns, which is far below the thermal time constant ($\tau_{\text{th}} \approx 26$ ms, see Table II), so the thermal state is approximately constant within each window. See Table III for a summary of these parameters.

Figure 10 summarizes the temperature dependence of Fuzzy entropy for two gain characteristic temperatures T_g. For strong gain–temperature coupling ($T_g = 50$ K), FE decreases systematically with increasing ambient temperature T_{amb}, and the class medians remain well separated. This indicates that thermal feedback strengthens history-dependent distortion as

---

[6] The absolute BER levels (on the order of 0.15–0.26 at 20 Gbps) are expected here because the receiver is intentionally simple and the device bandwidth and self-heating jointly induce substantial ISI.

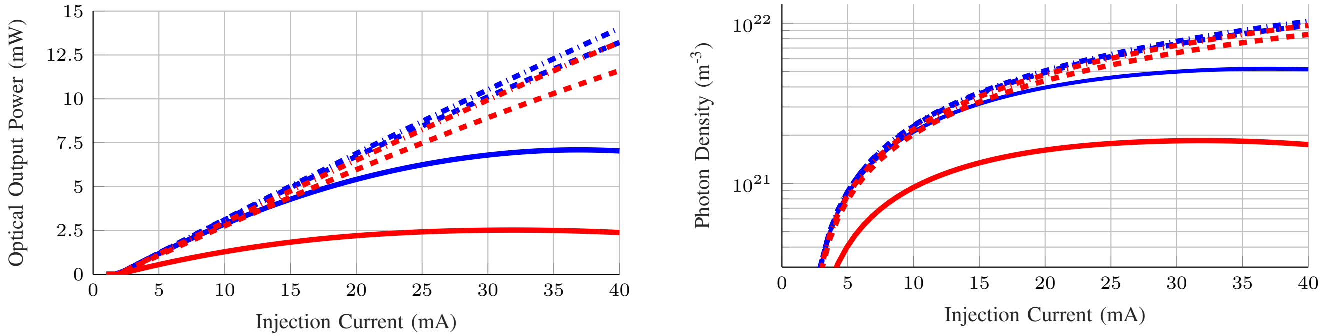

Fig. 4: Small-signal steady-state characteristics versus injection current. **Left**: Optical output power (L–I). **Right**: Photon density (log scale). Line style encodes gain–temperature sensitivity T_g: —— $T_g = 50\,\mathrm{K}$, - - - $T_g = 250\,\mathrm{K}$, -·-·· $T_g = 500\,\mathrm{K}$. Color encodes ambient temperature: —— $T_{\mathrm{amb}} = 25°\mathrm{C}$, —— $T_{\mathrm{amb}} = 90°\mathrm{C}$.

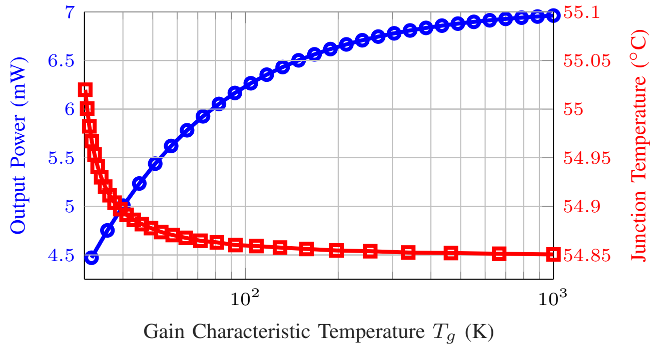

Fig. 5: Impact of gain characteristic temperature T_g on small-signal behavior at $I_{\mathrm{bias}} = 20$ mA and $T_{\mathrm{amb}} = 25°\mathrm{C}$ (simulation horizon 1 μs). Blue circles —— optical output power P_{opt} (left axis). Red squares —— junction temperature T_{j} (right axis).

the device heats. Interpreting FE as an unpredictability proxy, the observed decrease is consistent with increased pattern dependence: the slow thermal state restricts the set of admissible short-horizon trajectories of $P_{\mathrm{opt}}(t)$, so the output becomes more predictable and FE drops. For weak coupling ($T_g = 500$ K), FE changes only slightly with T_{amb} and the distributions largely overlap, consistent with dynamics dominated by the fast carrier–photon subsystem and only weakly conditioned on temperature history. Consequently, temperature inference from payload statistics is feasible only in the strong-coupling regime. These trends are also consistent with the BER results: configurations that are more thermally sensitive exhibit a stronger FE–temperature dependence.

To isolate the stochastic contribution to FE, we artificially degrade the default receive SNR of about 38 dB down to roughly -20 dB by injecting zero-mean Gaussian noise into each length-L window prior to feature extraction. Each noisy window is then scaled as in Sec. IV-A2 and processed by the same Fuzzy-entropy pipeline (see Table III). The results in Fig. 11 show a monotonic increase of FE as SNR decreases. From a dynamical system perspective, additive noise inflates inter-vector distances in the embedded space and reduces the probability that two k-histories that are close within radius r remain close after one-step extension. Using the approximation

$$\mathsf{FE}(k, r) \approx -\ln \mathbb{P}\big(\mathcal{B}_{k+1}(r) \mid \mathcal{B}_k(r)\big),$$

a decrease in this conditional probability yields a larger FE. In the high-SNR regime (inset), FE rises gently because noise perturbs near-threshold pairs while deterministic device dynamics still dominate. Below about 0 dB, the stochastic component governs one-step evolution and FE increases rapidly, progressively masking temperature contrast, as reflected by the narrowing separation between the 20°C and 25°C curves. Thus, at high SNR, FE primarily reflects deterministic thermal memory and remains temperature-informative, whereas under strong noise it largely tracks channel/front-end randomness and becomes temperature-uninformative. Taken together, these results indicate that the applicability of payload-based entropy analysis is governed by two distinct mechanisms. Weak gain–temperature coupling (large T_g) constitutes a fundamental limitation: when thermal feedback does not appreciably modulate the carrier–photon dynamics, the optical waveform carries little temperature-dependent structure, and no statistical post-processing can recover it. Reduced SNR primarily obscures otherwise present structure by elevating the entropy floor. In this case, temperature observability is not fundamentally lost but progressively masked by stochastic fluctuations, defining an operational SNR regime for reliable inference.

Alternative complexity measures based on multiscale coarse-graining and refined composite fuzzy entropy have been proposed to improve the stability of entropy estimates under noisy and short-length observations [55]; however, a systematic evaluation of such variants in the present VCSEL payload setting is beyond the scope of this work.

From an optical-device perspective, sweeping T_g performs a parametric study of the effective gain characteristic temperature, which aggregates microscopic gain roll-off, cavity detuning, and temperature-dependent internal losses. In the exponential law $g(T) = g_0 \exp\big(-(T - T_0)/T_g\big)$, the slope of $\ln g(T)$ with respect to T equals $-1/T_g$, so smaller T_g corresponds to pronounced thermo-gain sensitivity. In this regime, modest self-heating produces a substantial reduction of modal gain, drives the net gain toward zero, and accelerates roll-over in the L–I curve and photon density, consistent with Figs. 4 and 5. The rate equations then form a slow–fast system in which the junction temperature T_j is a slow variable that parametrically modulates the fast carrier–photon subsystem. The optical waveform is therefore strongly conditioned on T_j, and FE decreases because trajectories concentrate on a lower-

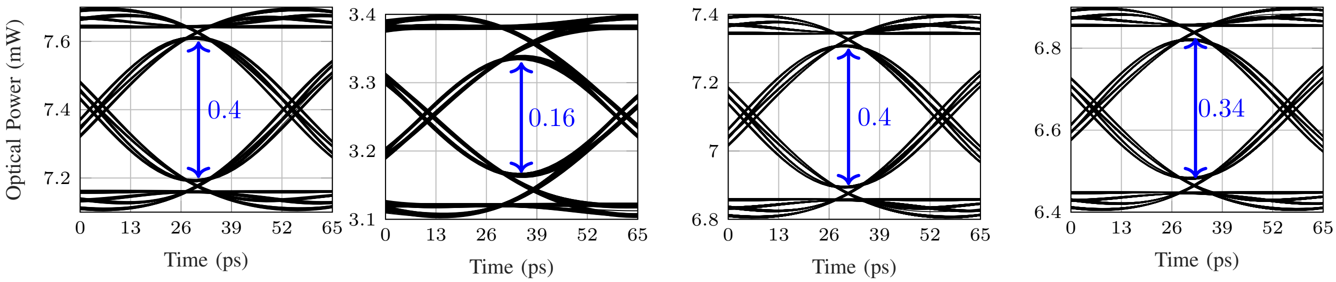

Fig. 6: Simulated eye diagrams of the VCSEL optical output under $R_b = 20$ Gb/s OOK signaling. From left to right, the panels correspond to $(T_g, T_{\mathrm{amb}}) = (50\ \mathrm{K}, 20^\circ\mathrm{C})$, $(50\ \mathrm{K}, 95^\circ\mathrm{C})$, $(500\ \mathrm{K}, 20^\circ\mathrm{C})$, and $(500\ \mathrm{K}, 95^\circ\mathrm{C})$. Blue arrows annotate the measured vertical eye opening at the sampling instant in each panel.

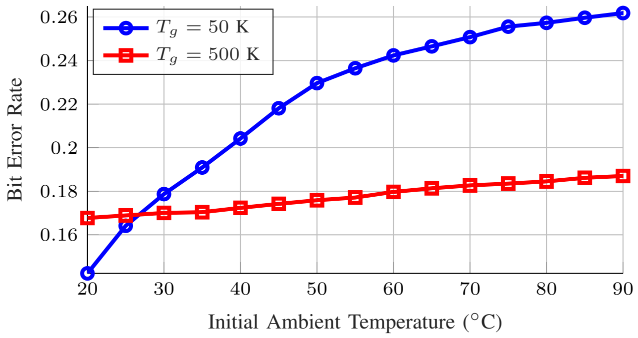

Fig. 7: BER versus ambient temperature for two gain characteristic temperatures T_g at $I_{\mathrm{bias}} = 20$ mA and $I_{\mathrm{mod}} = 5$ mA. BER is computed without equalization; absolute values are therefore not link-representative and are to illustrate relative temperature trends.

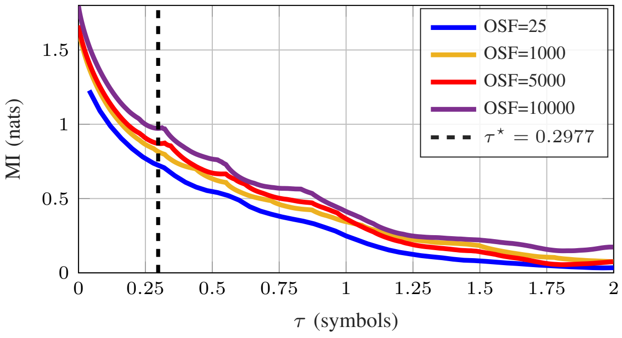

Fig. 8: AMI versus embedding delay τ (in symbols) for different OSF. The location of the first minimum, $\tau^\star \approx 0.30$ symbols, is robust across OSF and corresponds to $\tau \approx 7$ samples at OSF$= 25$.

dimensional manifold indexed by temperature. For larger T_g, $g(T)$ varies only weakly over the accessible thermal excursion, the carrier–photon dynamics are closer to linear and only weakly coupled to T_j, and FE becomes nearly temperature-invariant, being governed instead by the drive statistics and additive noise (cf. Fig. 11). In summary, the same parameter that optical designers use to quantify temperature sensitivity also governs the observability of junction temperature from payload data: strong gain–temperature coupling yields a temperature-informative, low-entropy waveform, whereas weak coupling yields a higher, noise-dominated entropy and sets a fundamental limit on pilot-free temperature inference in VCSEL.

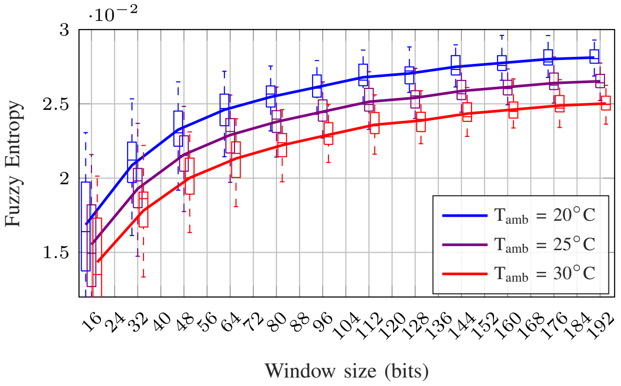

Fig. 9: Fuzzy entropy versus window size L for $T_g = 50$ K (fixed $I_{\mathrm{bias}} = 20$ mA, $I_{\mathrm{mod}} = 5$ mA, 20 Gbps).

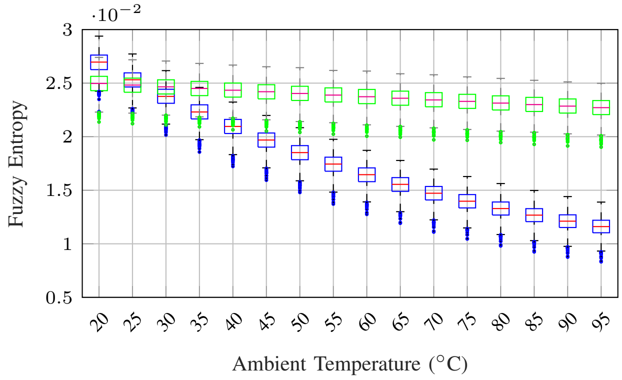

Fig. 10: Box plots of Fuzzy entropy versus ambient temperature for strong gain–temperature coupling ($T_g = 50$ K, blue) and weak coupling ($T_g = 500$ K, green).

E. Blind Temperature Regression

Following Sec. IV-A2, we train regressors of the form $\hat{T} = \mathcal{R}(\mathrm{FE})$ using Fuzzy entropy features extracted from $P_{\mathrm{opt}}(t)$ (cf. Table III). Table IV reports mean absolute error (MAE), root mean square error (RMSE), and coefficient of determination (R^2) for $T_g \in \{50, 500\}$.

At strong coupling ($T_g = 50$ K), Gaussian process regression (GPR) achieves the best accuracy (MAE $\approx 3.7^\circ$C, RMSE $\approx 4.8^\circ$C, $R^2 \approx 1.0$), with Random Forest and a shallow multi-layer perceptron performing comparably. These results confirm that FE alone provides a temperature-informative, nonlinear feature under thermally coupled dynamics. By contrast, at weak coupling ($T_g = 500$ K), all models degrade sharply

TABLE IV: Regression Performance at T_g=50 K and T_g=500 K. Lower is better for MAE/RMSE; higher is better for R^2. Features: Fuzzy entropy from $P_{\mathrm{opt}}(t)$ with k=2, n=3, r=0.2 std, window L=128 bits.

	TG = 50			TG = 500		
Model	MAE	RMSE	R^2	MAE	RMSE	R^2
Gaussian Process	**3.7**	**4.8**	**1.0**	**15.3**	**18.6**	**0.4**
Linear Regression	12.5	14.4	0.6	19.8	22.8	0.0
Multi-Layer Perceptron	4.6	5.8	0.9	15.4	18.7	0.3
Random Forest	4.0	5.2	0.9	16.4	20.3	0.2
Support Vector Regression (RBF)	5.6	7.2	0.9	19.5	22.5	0.1

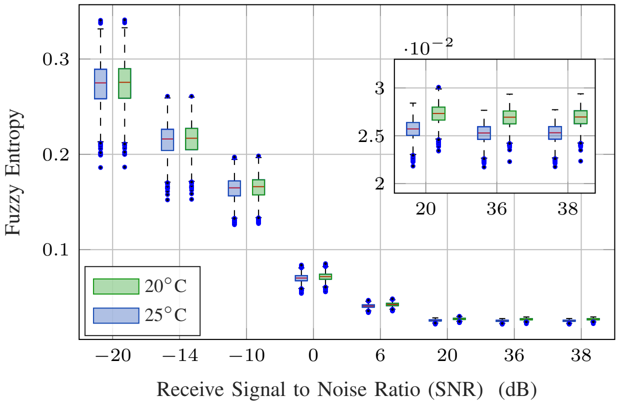

Fig. 11: Fuzzy entropy versus receive SNR for strong coupling (T_g = 50 K) at two ambient temperatures (20°C and 25°C).

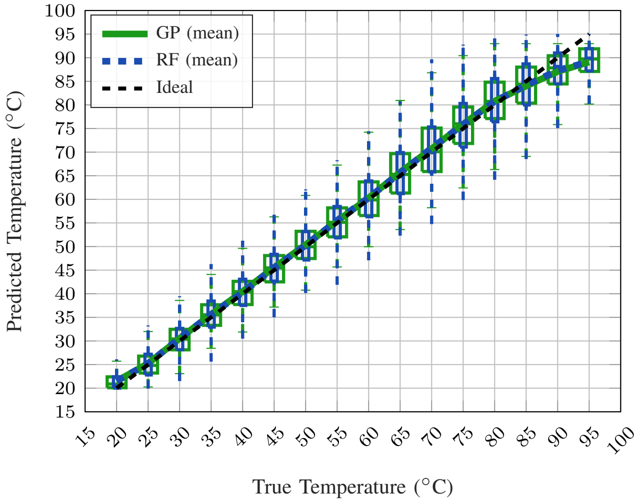

Fig. 12: Predicted vs. true temperature for the best regressors at T_g=50 K. Boxes show interquartile ranges across Monte Carlo realizations and ambient temperatures.

(e.g., GPR: MAE ≈ 15.3°C, $R^2 \approx 0.35$), reflecting the weak dependence of FE on temperature when the device behaves nearly linearly (cf. Fig.7).

Figure 12 illustrates predicted versus true temperatures for the two best learners (GPR and Random Forest) at $T_g = 50$ K. Predictions align closely with the diagonal, with interquartile ranges concentrated around the mean. A mild heteroscedastic spread is observed at high temperatures, attributed to dynamic-range compression of entropy and increased waveform variability near thermal roll-over. A slight underestimation at the hottest points is consistent with saturation of FE. These outcomes confirm that Fuzzy entropy of the received waveform can serve as a pilot-free proxy for internal temperature, provided that temperature–gain coupling is appreciable.

VI. CONCLUSION

We have proposed a pilot-free method for estimating the internal temperature of VCSELs by exploiting the statistical complexity of their payload waveform. Building on the electro–thermal rate-equation model, we hypothesized that thermal feedback introduces long-term dependencies into the optical output, which can be quantified through Fuzzy entropy as a single temperature-informative feature. The approach requires no pilots, embedded sensors, or transmitter-side data, making it directly applicable for in-service monitoring.

Simulation results confirmed this hypothesis: under strong temperature–gain coupling ($T_g = 50$ K), Fuzzy entropy decreases monotonically with increasing ambient temperature, enabling accurate regression with Gaussian Process models achieving sub-5°C RMSE. In contrast, for weak coupling ($T_g = 500$ K), the entropy–temperature relationship is flat and regression performance degrades, consistent with the reduced thermal sensitivity of the dynamics. Additional simulations with injected noise showed that Fuzzy entropy increases when stochastic fluctuations dominate, highlighting the method's operating regime and limitations.

Overall, these findings demonstrate that entropy-based payload analysis provides a viable, low-cost proxy for monitoring internal thermal dynamics in high-speed optical interconnects when thermal coupling is appreciable. Future work includes extending the framework to driver and receiver circuitry, moving beyond isolated device dynamics to capture full transceiver behavior.

REFERENCES

[1] M. Srinivasan, J. Song, A. Grabowski, K. Szczerba, H. K. Iversen, M. N. Schmidt, D. Zibar, J. Schröder, A. Larsson, C. Häger *et al.*, "End-to-end learning for VCSEL-based optical interconnects: State-of-the-art, challenges, and opportunities," *Journal of Lightwave Technology*, vol. 41, no. 11, pp. 3261–3277, 2023.

[2] R. Michalzik, "VCSEL fundamentals," in *VCSELs: fundamentals, technology and applications of vertical-cavity surface-emitting lasers*. Springer, 2012, pp. 19–75.

[3] M. B. Aziz, H. D. Kaimre, and P. Andrekson, "High-speed transmission of 850 nm VCSEL optical interconnects across wide temperatures," *IEEE Photonics Technology Letters*, p. 1, 2024.

[4] L. Qin, J. Ren, and X.-S. Xu, "Optoelectronic properties of vertical-cavity surface-emitting laser at low temperature," *Acta Physica Sinica*, vol. 68, no. 19, 2019.

[5] P. S. Menon, K. Kumarajah, M. Ismail, B. Y. M. Majlis, and S. Shaari, "Long-wavelength MQW vertical-cavity surface emitting laser: Effects of lattice temperature," *Journal of Optical Communications*, vol. 31, no. 2, pp. 81–84, 2010.

[6] H. D. Kaimre, A. Grabowski, J. Gustavsson, and A. Larsson, "25 Gbaud 850 nm VCSEL for an extended temperature range," *IEEE Photonics Technology Letters*, 2025.

[7] K. M. Krishna and M. G. Madhan, "Performance analysis of a low cost VCSEL transmitter based multimode fiber optic link for gigabit ethernet application," in *2016 International Conference on Communication and Signal Processing (ICCSP)*. IEEE, 2016, pp. 0270–0274.

[8] T. Zhang, J. Dai, and Z. Wang, "Analysis of temperature characteristics of high power vertical cavity surface emitting laser arrays," in *Fourteenth International Conference on Information Optics and Photonics (CIOP 2023)*, vol. 12935. SPIE, 2023, pp. 513–521.

[9] A. Grabowski, J. Gustavsson, Z. S. He, and A. Larsson, "Large-signal equivalent circuit for datacom vcsels," *Journal of Lightwave Technology*, vol. 39, no. 10, pp. 3225–3233, 2021.

[10] P. V. Mena, J. J. Morikuni, S.-M. Kang, A. V. Harton, and K. W. Wyatt, "A simple rate-equation-based thermal VCSEL model," *Journal of Lightwave Technology*, vol. 17, no. 5, pp. 865–872, 1999.

[11] M. Daubenschuez and R. Michalzik, "Parameter extraction from temperature-dependent light–current–voltage data of vertical-cavity surface-emitting lasers," in *Semiconductor Lasers and Laser Dynamics VII*, vol. 9892. SPIE, 2016.

[12] J. H. Lee, J. H. Moon, P.-C. Su, and S. H. Lee, "Numerical analysis of injected current effects on thermal characteristics of vertical-cavity surface-emitting laser," *Journal of Mechanical Science and Technology*, vol. 32, pp. 1463–1469, 2018.

[13] J. Yan, J. Wang, C. Tang, X. Liu, G. Zhang, and Y. He, "An electrooptothermal-coupled circuit-level model for VCSELs under pulsed condition," *IEEE Transactions on Industrial Electronics*, vol. 66, no. 2, pp. 1315–1324, 2019.

[14] K. Choquette, "Vertical cavity surface emitting lasers (VCSELs)," in *Semiconductor Lasers*. Elsevier, 2013, pp. 316–340.

[15] A. Filipchuk, K. Nechay, R. Ulkuniemi, S. Talmila, and P. Uusimaa, "Thermal management optimization in high-power 3D sensing VCSELs," in *Proceedings of SPIE, Components and Packaging for Laser Systems VIII*, vol. 11982, 2022, pp. 84–89.

[16] M. Schmid, M. Momberg, M. Kettelgerdes, and G. Elger, "Transient thermal analysis for VCSEL diodes," in *Proceedings of the 2023 29th International Workshop on Thermal Investigations of ICs and Systems (THERMINIC)*, 2023.

[17] C. Cengiz, M. Azarifar, and M. Arik, "A critical review on the junction temperature measurement of light emitting diodes," *Micromachines*, vol. 13, no. 10, p. 1615, 2022.

[18] F. Zhang, Z. Xu, S. Jiang, J. Ni, Q. Zhao, and C. Wang, "Ultrahigh-resolution and large-dynamic-range temperature sensor based on fiber-optic EFPI cavity," *IEEE Sensors Journal*, vol. 23, no. 7, pp. 6857–6863, 2023.

[19] A. Ghods, M. Yeo, J. Gariano, W. Lawal, and S. Agrawal, "Advanced characterization of 795nm VCSELs for atomic clock applications," in *Quantum Information Science, Sensing, and Computation XVII*, vol. 13451. SPIE, 2025, pp. 15–19.

[20] G. P. Miroshnichenko, A. N. Arzhanenkova, and M. Y. Plotnikov, "Investigation of the method of current thermal modulation of the wavelength VCSEL," *Nanosystems: Physics, Chemistry, Mathematics*, vol. 13, no. 6, pp. 615–620, 2022.

[21] I. Khan, L. Tunesi, M. U. Masood, E. Ghillino, A. Carena, V. Curri, and P. Bardella, "Machine learning assisted extraction of vertical cavity surface emitting lasers parameters," in *2022 IEEE Photonics Conference (IPC)*. IEEE, 2022, pp. 1–2.

[22] I. Khan, M. U. Masood, L. Tunesi, E. Ghillino, A. Carena, V. Curri, and P. Bardella, "Two-step machine learning assisted extraction of VCSEL parameters," in *Physics and Simulation of Optoelectronic Devices XXXI*, vol. 12415. SPIE, 2023, pp. 159–162.

[23] M. Srinivasan, A. Pourafzal, S. Giannakopoulos, P. Andrekson, C. Häger, and H. Wymeersch, "Learning gradient-based feed-forward equalizer for VCSELs," in *Photonics*, vol. 11, no. 10. MDPI, 2024, p. 943.

[24] Y. He, X. Jin, P. Jin, J. Su, F. Li, and H. Lu, "Temperature control performance improvement of high-power laser diode with assistance of machine learning," in *Photonics*, vol. 12, no. 3. MDPI, 2025, p. 241.

[25] W. Chen, Z. Wang, H. Xie, and W. Yu, "Characterization of surface emg signal based on fuzzy entropy," *IEEE Transactions on neural systems and rehabilitation engineering*, vol. 15, no. 2, pp. 266–272, 2007.

[26] K. Safarihamid, A. Pourafzal, and A. Fereidunian, "A joint-entropy approach to time-series classification," in *2021 7th International Conference on Signal Processing and Intelligent Systems (ICSPIS)*. IEEE, 2021, pp. 1–7.

[27] H. D. Kaimre, A. Grabowski, J. Gustavsson, and A. Larsson, "Effects of detuning on wide-temperature behavior of 25 Gbaud 850nm VCSELs," in *Vertical-Cavity Surface-Emitting Lasers XXVII*, vol. 12439. SPIE, 2023.

[28] C. Qi, X. Shi, and G. Wang, "Thermal circuit model of MQW VCSEL laser," in *Proceedings of the 2010 International Conference on Microwave and Millimeter Wave Technology (ICMMT)*, 2010, pp. 1498–1501.

[29] M. Karray, P. Desgreys, and J.-J. Charlot, "VHDL-AMS modeling of VCSEL including noise," in *Proceedings of the 2003 IEEE Conference on Design and Test of Integrated Systems in Nanoscale Technology*, 2003, pp. 118–121.

[30] X. Shi, C. Qi, G. Wang, J. Hu, and F. Liu, "Multimode rate-equation-based VCSEL thermal and spatial model of circuit level," in *Proceedings of the 2010 International Conference on Measuring Technology and Mechatronics Automation (ICMTMA)*, vol. 3, 2010, pp. 402–405.

[31] D. M. Byrne and B. A. Keating, "A laser diode model based on temperature dependent rate equations," *IEEE photonics technology letters*, vol. 1, no. 11, pp. 356–359, 1989.

[32] Y.-y. Fei, X.-d. Meng, M. Gao, Y. Yang, H. Wang, and Z. Ma, "Strong light illumination on gain-switched semiconductor lasers helps the eavesdropper in practical quantum key distribution systems," *Optics Communications*, vol. 419, pp. 83–89, 2018.

[33] S. H. Strogatz, *Nonlinear Dynamics and Chaos: With Applications to Physics, Biology, Chemistry, and Engineering*, 2nd ed. CRC Press, 2018.

[34] A. Fereidunian, H. Lesani, M. A. Zamani, M. A. S. Kolarijani, N. Hassanpour, and S. S. Mansouri, "A complex adaptive system of systems approach to human–automation interaction in smart grid," *Contemporary issues in systems science and engineering*, pp. 425–500, 2015.

[35] C. E. Shannon, "A mathematical theory of communication," *The Bell system technical journal*, vol. 27, no. 3, pp. 379–423, 1948.

[36] J. P. Crutchfield and K. Young, "Inferring statistical complexity," *Physical Review Letters*, vol. 63, no. 2, pp. 105–108, 1989.

[37] J. P. Crutchfield, "Between order and chaos," *Nature Physics*, vol. 8, no. 1, pp. 17–24, 2012.

[38] P. Walters, *An Introduction to Ergodic Theory*, ser. Graduate Texts in Mathematics. Springer, 1982, vol. 79.

[39] F. Takens, "Detecting strange attractors in turbulence," in *Dynamical Systems and Turbulence, Warwick 1980: proceedings of a symposium held at the University of Warwick 1979/80*. Springer, 2006, pp. 366–381.

[40] P. Grassberger and I. Procaccia, "Characterization of strange attractors," *Physical review letters*, vol. 50, no. 5, p. 346, 1983.

[41] H. Kantz and T. Schreiber, *Nonlinear Time Series Analysis*, 2nd ed. Cambridge: Cambridge University Press, 2010.

[42] S. M. Pincus, "Approximate entropy as a measure of system complexity." *Proceedings of the national academy of sciences*, vol. 88, no. 6, pp. 2297–2301, 1991.

[43] B. S. Thomson, J. B. Bruckner, and A. M. Bruckner, *Elementary real analysis*. ClassicalRealAnalysis. com, 2008, vol. 1.

[44] G. P. Agrawal, *Fiber-Optic Communication Systems*, 4th ed. Wiley-Blackwell, 2010.

[45] A. M. Fraser and H. L. Swinney, "Independent coordinates for strange attractors from mutual information," *Physical review A*, vol. 33, no. 2, p. 1134, 1986.

[46] C. M. Bishop, *Pattern recognition and machine learning*. Springer, 2006, vol. 4, no. 4.

[47] X. Yin, J. Bauwelinck, X.-Z. Qiu, and J. Vandewege, "A second-order feedforward optical power control scheme for automotive vcsel drivers," *IEEE Photonics Technology Letters*, vol. 22, no. 22, pp. 1683–1685, 2010.

[48] W.-S. Oh, K.-Y. Park, and S. Lee, "A 4-ch 10-gb/s cmos vcsel driver array with adaptive optical power control," in *2010 The 12th International Conference on Advanced Communication Technology (ICACT)*, vol. 1. IEEE, 2010, pp. 826–829.

[49] O. Ueda and S. J. Pearton, "Materials and reliability handbook for semiconductor optical and electron devices," 2013.

[50] J. Piprek, *Semiconductor optoelectronic devices: introduction to physics and simulation*. Academic press, 2003.

[51] K. H. Rhew, S. C. Jeon, D. H. Lee, B.-S. Yoo, and I. Yun, "Reliability assessment of 1.55-μm vertical cavity surface emitting lasers with tunnel junction using high-temperature aging tests," *Microelectronics Reliability*, vol. 49, no. 1, pp. 42–50, 2009. [Online]. Available: https://www.sciencedirect.com/science/article/pii/S0026271408003831

[52] K. Kaeval, T. Fehenberger, J. Zou, S. L. Jansen, K. Grobe, H. Griesser, J.-P. Elbers, M. Tikas, and G. Jervan, "Qot assessment of the optical spectrum as a service in disaggregated network scenarios," *Journal of*

optical communications and networking, vol. 13, no. 10, pp. E1–E12, 2021.

[53] Y. Ohiso, K. Tateno, Y. Kohama, A. Wakatsuki, H. Tsunetsugu, and T. Kurokawa, "Flip-chip bonded 0.85-μm bottom-emitting vertical-cavity laser array on an algaas substrate," *IEEE Photonics Technology Letters*, vol. 8, no. 9, pp. 1115–1117, 1996.

[54] A. S. Tanenbaum, *Computer networks*. Pearson Education India, 2003.

[55] H. Azami and J. Escudero, "Refined composite multivariate generalized multiscale fuzzy entropy: A tool for complexity analysis of multichannel signals," *Physica A: Statistical Mechanics and its Applications*, vol. 465, pp. 261–276, 2017.

Alireza Pourafzal (Member, IEEE) received his Bachelor's degree in Electrical Engineering in 2016 and his Master's degree in Wireless Communications in 2019 from K.N. Toosi University of Technology in Iran. He earned his PhD in Information and Communication Technology in 2023 from the Norwegian University of Science and Technology (NTNU). He is currently a Postdoctoral Researcher in the Communication Group at Chalmers University of Technology, Sweden. His research interests include array signal processing, channel estimation, DOA estimation, and machine learning for wireless and optical communications.

Christian Häger is an Associate Professor in the Department of Electrical Engineering at Chalmers University of Technology, Sweden. He received the Dipl.-Ing. degree (M.Sc. equivalent) from Ulm University, Germany, in 2011 and his Ph.D. degree from Chalmers University of Technology, Sweden, in 2016. He was a postdoctoral researcher at the Department of Electrical and Computer Engineering at Duke University, USA and at the Department of Electrical Engineering at Chalmers University of Technology. His research interests lie at the intersection of communication systems, machine learning, and signal processing. He received the Marie Sklodowska-Curie Global Fellowship from the European Commission in 2017 and a Starting Grant from the Swedish Research Council in 2020.

Peter Andrekson (Life Fellow, IEEE) received his Ph.D. from Chalmers University of Technology, Sweden, in 1988. After about three years with AT&T Bell Laboratories, Murray Hill, N.J., he returned to Chalmers where he is a full professor at the Department of Microtechnology and Nanoscience. He was Director of Research at Cenix Inc. in Allentown, PA, USA, during 2000 – 2003. His research interests include many aspects of fiber communications such as optical amplifiers, nonlinear pulse propagation, all-optical functionalities, and high spectral efficiency transmission. He is co-founder of the optical test & measurement company Picosolve Inc., now part of EXFO. Andrekson is a Fellow of OSA, IEEE and the Royal Swedish Academy of Engineering Sciences (IVA). He held an ERC Advanced Grant for work on phase-sensitive optical amplifiers (2012-2017) and is currently a distinguished professor by the Swedish Research Council (VR). He was the director of the Fibre Optic Communications Research Centre (FORCE) at Chalmers during 2010-2025.

Henk Wymeersch (Fellow, IEEE) received the Ph.D. degree in electrical engineering/applied sciences from Ghent University, Ghent, Belgium, in 2005. He is currently a Professor of communication systems with the Department of Electrical Engineering, Chalmers University of Technology, Gothenburg, Sweden. From 2005 to 2009, he was a Postdoctoral Researcher with the Laboratory for Information and Decision Systems, Massachusetts Institute of Technology, Cambridge, MA, USA. His research interests include the convergence of communication and sensing in a 5G and Beyond 5G context. He was an Associate Editor for IEEE COMMUNICATION LETTERS from 2009 to 2013, IEEE TRANSACTIONS ON WIRELESS COMMUNICATIONS since 2013, and IEEE TRANSACTIONS ON COMMUNICATIONS from 2016 to 2018. He is also a Senior Member of the IEEE Signal Processing Magazine Editorial Board. During 2019–2021, he was an IEEE Distinguished Lecturer with the Vehicular Technology Society.